

SURFACE BRIGHTNESS PROFILES OF COMPOSITE IMAGES OF COMPACT GALAXIES AT $z \simeq 4-6$ IN THE HUDF

N. P. HATHI¹, R. A. JANSEN^{2,1}, R. A. WINDHORST^{2,1}, S. H. COHEN²,
 W. C. KEEL³, M. R. CORBIN⁴ AND R. E. RYAN JR.¹

Draft version February 9, 2022

ABSTRACT

The Hubble Ultra Deep Field (HUDF) contains a significant number of B -, V - and i' -band dropout objects, many of which were recently confirmed to be young star-forming galaxies at $z \simeq 4-6$. These galaxies are too faint individually to accurately measure their radial surface brightness profiles. Their average light profiles are potentially of great interest, since they may contain clues to the time since the onset of significant galaxy assembly. We separately co-add V , i' - and z' -band HUDF images of sets of $z \simeq 4, 5$ and 6 objects, pre-selected to have nearly identical compact sizes and the roundest shapes. From these stacked images, we are able to study the average(d) radial structure of these objects at much higher signal-to-noise ratio than possible for an individual faint object. Here we explore the reliability and usefulness of a stacking technique of compact objects at $z \simeq 4-6$ in the HUDF. Our results are: (1) image stacking provides reliable and reproducible average surface brightness profiles; (2) the shape of the average surface brightness profile shows that even the faintest $z \simeq 4-6$ objects are *resolved*; and (3) if late-type galaxies dominate the population of galaxies at $z \simeq 4-6$, as previous *HST* studies have shown for $z \lesssim 4$, then limits to dynamical age estimates for these galaxies from their profile shapes are comparable with the SED ages obtained from the broadband colors. We also present accurate measurements of the sky-background in the HUDF and its associated 1σ uncertainties.

Subject headings: galaxies: high-redshift — galaxies: structure — galaxies: formation

1. INTRODUCTION

In the last decade, ground and space based observations of high redshift galaxies have begun to outline the process of galaxy assembly. The details of that process at high redshifts, however, remain poorly constrained. There is increasing support for the model of galaxy formation, in which the most massive galaxies assemble earlier than their less massive counterparts (e.g. Cowie et al. 1996; Guzman et al. 1997; Kodama et al. 2004; McCarthy et al. 2004). A detailed analysis of the ‘fossil record’ of the current stellar populations in nearby galaxies selected from the *Sloan Digital Sky Survey* (SDSS; York et al. 2000) provides strong evidence for this downsizing picture (Heavens et al. 2004; Panter et al. 2007). The increasing number of luminous galaxies spectroscopically confirmed to be at $z \simeq 6.5$ (e.g. Hu et al. 2002; Kodaira et al. 2003; Kurk et al. 2004; Rhoads et al. 2004; Stern et al. 2005; Taniguchi et al. 2005), or $\lesssim 0.9$ Gyr after the Big Bang, also supports this general picture. In an alternate hierarchical scenario, arguments have been made that significant number of low luminosity dwarf galaxies were present at these times, and were the main contributor to finish the process of reionization of the intergalactic medium (Yan & Windhorst 2004a,b). However, there is presently little information on the dynamical structure of these or other galaxies at $z \simeq 6$.

It is not clear whether these objects represent isolated disk systems, or collapsing spheroids, mergers or other dynamically young objects.

Ravindranath et al. (2006) used deep, multi-wavelength images obtained with the *Hubble Space Telescope* (*HST*) Advanced Camera for Surveys (ACS) as part of the Great Observatories Origins Deep Survey (GOODS) to analyze 2-D surface brightness distributions of the brightest Lyman Break Galaxies (LBGs) at $2.5 < z < 5$. They distinguish various morphologies based on the Sérsic index n , which measures the shape of the azimuthally averaged surface brightness profile (where $n=1$ for exponential disks and $n=4$ for a de Vaucouleurs law). Ravindranath et al. (2006) find that 40% of the LBGs have light profiles close to exponential, as seen for disk galaxies, and only $\sim 30\%$ have high n , as seen in nearby spheroids. They also find a significant fraction ($\sim 30\%$) of galaxies with light profiles *shallower* than exponential, which appear to have multiple cores or disturbed morphologies, suggestive of close pairs or on-going galaxy mergers. Distinction between these possible morphologies and, therefore, a better estimate of the formation redshifts of the systems observed at $z \simeq 4-6$ in particular, is important for testing the galaxy assembly picture, and for the refinement of galaxy formation models.

One possible technique involves the radial surface brightness profiles of the most massive objects — those that will likely evolve to become the massive elliptical galaxies, which we see in place at redshifts $z \lesssim 2$ (Driver et al. 1998; van Dokkum et al. 2003, 2004). This can be analytically understood in the context of the Lynden-Bell (1967) relaxation formalism and the numerical galaxy formation simulations of van Albada (1982), which describe collisionless collapse and violent relax-

Electronic address: Nimish.Hathi@asu.edu

¹ Department of Physics, Arizona State University, Tempe, AZ 85287-1504, USA

² School of Earth and Space Exploration, Arizona State University, Tempe, AZ 85287-1404, USA

³ Department of Physics and Astronomy, University of Alabama, Box 870324, Tuscaloosa, AL 35487, USA

⁴ U. S. Naval Observatory, 10391 W. Naval Observatory Road, Flagstaff, AZ 86001-8521, USA

ation as the formation mechanism for elliptical galaxies. As the time-scale for relaxation is shorter in the inner than in the outer parts of a galaxy, convergence toward a $r^{1/n}$ -profile will proceed from the inside to progressively larger radii at later times. Moreover, Kormendy (1977) has shown that tidal perturbations due to neighbors can cause the radial surface brightness profile to deviate from a pure de Vaucouleurs profile in the outer parts of a galaxy. This implies that the radius where surface brightness profiles start to deviate significantly from an $r^{1/n}$ profile *might* serve as a “virial clock” that traces the time since the onset of the last major merger, accretion events or global starburst in these objects.

Image stacking methods have been used extensively on X-ray (Nandra et al. 2002; Brandt et al. 2001) and radio (Georgakakis et al. 2003; White et al. 2007) data to study the mean properties (e.g. flux, luminosity) of well-defined samples of sources that are otherwise too faint to be detected individually. Pascarelle et al. (1996) applied such a stacking method to a large number of optically very faint, compact objects at $z = 2.39$ to trace their “average” structure. This approach was also applied by Zibetti et al. (2004) to detect the presence of faint stellar halos around disk galaxies selected from the SDSS. An attempt to apply this technique to high redshift galaxies in the Hubble Deep Field (HDF; Williams et al. 1996) was not conclusive (H. Ferguson; private communication) due to the poorer spatial sampling and shallower depth of the HDF compared to the Hubble Ultra Deep Field (HUDF; Beckwith et al. 2006).

In this paper, we use the exceptional depth and fine spatial sampling of the HUDF to study the potential of this image stacking technique, and will estimate limits to dynamical ages of faint, young galaxies at $z \simeq 4-6$. The HUDF reaches ~ 1.5 mag deeper than the equivalent HDF exposure in the i' -band, and has better spatial sampling than the HDF. The HUDF depth also allows us to characterize the sky background very accurately, which is critical for successfully using a stacking method to measure the mean surface-brightness profiles for these faint young galaxies.

This paper is organized as follows: In § 2 we summarize the HUDF observations, and in § 3 we discuss the selection of our $z \simeq 4, 5$ and 6 samples. In § 4 we describe our data analysis, which includes accurately measuring the 1σ sky-subtraction error, the image stacking method to generate mean surface-brightness profiles, and our test of its reliability. In § 5 we present and discuss our results in terms of the average surface-brightness profiles of $z \simeq 4-6$ galaxies, and in § 6 we conclude with a summary of our results.

Throughout this paper we refer to the *HST*/ACS F435W, F606W, F775W, and F850LP filters as the B -, V -, i' -, and z' -bands, respectively. We assume a *Wilkinson Microwave Anisotropy Probe* (WMAP) cosmology of $\Omega_m=0.24$, $\Omega_\Lambda=0.76$ and $H_0=73$ km s $^{-1}$ Mpc $^{-1}$, in accord with the most recent 3-year WMAP results of Spergel et al. (2007). This implies a current age for the Universe of 13.65 Gyr. All magnitudes are given in the AB system (Oke & Gunn 1983).

2. OBSERVATIONS

The HUDF contains $\gtrsim 100$ objects that are i' -band dropouts, making them candidates for galaxies at $z \simeq$

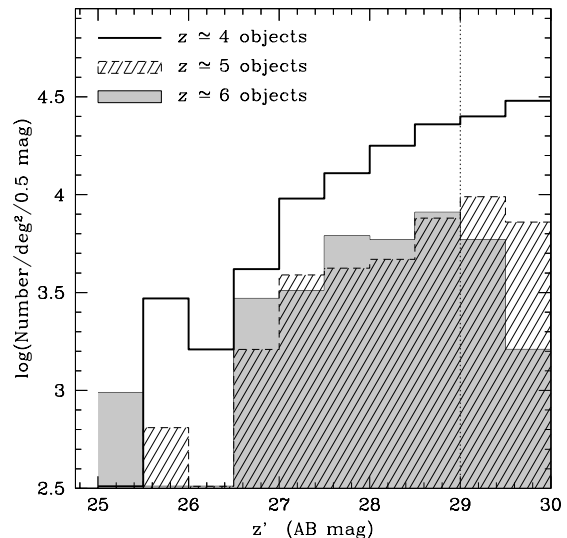


FIG. 1.— The HUDF number counts for all $z \simeq 4, 5, 6$ objects before the sub-selection of compact isolated $z \simeq 4, 5, 6$ objects was made. The vertical dotted line shows the magnitude to which the number counts of all these redshifts are complete. The area of the HUDF is 3.15×10^{-3} deg 2 .

6 (Bouwens et al. 2004, 2006; Bunker & Stanway 2004; Yan & Windhorst 2004b). Similarly, there are larger numbers of objects in the HUDF that are B -band dropouts (415 in total) or V -band dropouts (265 in total), and are candidates for galaxies at $z \simeq 4$ and $z \simeq 5$, respectively. Beckwith et al. (2006) and Bouwens et al. (2007) find similar number of B - and V -band dropouts in the HUDF. A significant fraction of these objects to $AB \lesssim 27$ mag have recently been spectroscopically confirmed to have redshifts $z \simeq 4-6$ through the detection of Ly α emission or identifying their Lyman break (Malhotra et al. 2005; Dow-Hygelund et al. 2007). We discuss our detailed drop-out selection criteria below. Despite the depth ($AB \lesssim 29.5$ mag) of the HUDF images, however, these objects appear very faint and with little, if any, discernible structural detail. Visual inspection of all these objects shows their morphologies to divide into four broad categories: symmetric, compact, elongated, and amorphous.

3. SAMPLE SELECTION

We construct three separate catalogs for these $z \simeq 4, 5, 6$ galaxy candidates, selecting only the *isolated*, *compact* and *symmetric* galaxies. We exclude objects with obvious nearby neighbors, to avoid a bias due to dynamically disturbed objects and complications due to chance superpositions. Figure 1 demonstrates that our completeness limit for $z \simeq 4$ and $z \simeq 5$ objects is $AB \lesssim 29.3$ mag, and for $z \simeq 6$ objects it is $AB \lesssim 29.0$ mag. Therefore, all three catalogs are complete to $AB \lesssim 29.0$ mag, which is equivalent to at least a 10σ detection for objects that are nearly point sources. For each object in our $z \simeq 4, 5, 6$ samples, we extracted 51×51 pixel postage stamps (which at $0''.03$ pix $^{-1}$ span $1''.53$ on a side) from the HUDF V , i' and z' -band images, respectively. Each postage stamp was extracted from the full HUDF, such that the centroid of an object (usually coincident with the brightest pixel) was at the center of that stamp.

3.1. The $z \simeq 4$ and $z \simeq 5$ Objects (B -, V -band dropouts)

We used the i' -band selected $BVi'z'$ HUDF catalog (Beckwith et al. 2006) to select the $z \simeq 4$ and $z \simeq 5$ objects. With the *HyperZ* code (Bolzonella et al. 2000), we computed photometric redshift estimates, using the magnitudes and associated uncertainties tabulated in the HUDF catalog. All objects with $3.5 \leq z_{\text{phot}} \leq 4.5$ were assigned to the bin of $z \simeq 4$ candidates, and all objects with $4.5 \leq z_{\text{phot}} \leq 5.5$ to the bin of $z \simeq 5$ candidates.

We then applied color criteria, similar to those adopted by Giavalisco et al. (2004), to select the $B(z \simeq 4)$ and $V(z \simeq 5)$ dropout samples. For B -band dropouts, we require:

$$\begin{cases} (B - V) \geq 1.2 + 1.4 \times (V - z') \text{ mag} \\ \text{and } (B - V) \geq 1.2 \text{ mag} \\ \text{and } (V - z') \leq 1.2 \text{ mag} \end{cases}$$

For V -band dropouts, the following color selection was applied:

$$\begin{cases} (V - i') > 1.5 + 0.9 \times (i' - z') \text{ or } (V - i') > 2.0 \text{ mag} \\ \text{and } (V - i') \geq 1.2 \text{ mag} \\ \text{and } (i' - z') \leq 1.3 \text{ mag} \end{cases}$$

We note, that only objects satisfying *both* color *and* photometric redshift criteria were selected in our samples. Vanzella et al. (2006) using VLT/FORS2 observed ~ 100 B -, V - and i' -band dropout objects in the Chandra Deep Field South (CDFs) selected based on above mentioned color criteria (Giavalisco et al. 2004). They have spectroscopically confirmed $>90\%$ of their high redshift galaxy candidates. Therefore, we expect only a small number ($<10\%$) of contaminants in our sample of dropouts. One or two objects in our final sample could be such contaminants, but because we have 3 different realizations of 10 objects (3×10), each showing similar profiles, they do not appear to affect our results.

The $z \simeq 4$ sample has 415 objects, while the $z \simeq 5$ sample has 265 objects. In Figure 2ab, we show the distribution of the FWHM and ellipticity, $\epsilon = (1 - b/a)$, measured in each of the two samples using *SExtractor* (Bertin & Arnouts 1996). We further constrained our samples by imposing limits on compactness and on roundness of FWHM $\leq 0''.3$ and $\epsilon \leq 0.3$. Again, this is to minimize the probability that the $z \simeq 4-5$ candidates are significantly dynamically disturbed, and to maximize the probability of selecting physically similar objects. Our goal is to find the visibly most symmetric, least disturbed systems for the current study. This sub-selection leaves 204 objects in the $z \simeq 4$ sample and 102 objects in the $z \simeq 5$ sample. Most of these objects are faint, and are only a few pixels across in size, and, hence, have larger uncertainties in their measurements of FWHM and ellipticity. Therefore, we also checked our objects visually to eliminate any possibility of our selected objects being contaminated by unrelated nearby objects, being clearly extended, or objects with complex morphologies.

3.2. $z \simeq 6$ Objects (i' -band dropouts)

Yan & Windhorst (2004b) found 108 possible $5.5 \leq z \leq 6.5$ candidates in the HUDF to $m_{AB}(z_{850}) = 30.0$ mag. Bunker & Stanway (2004) independently found the

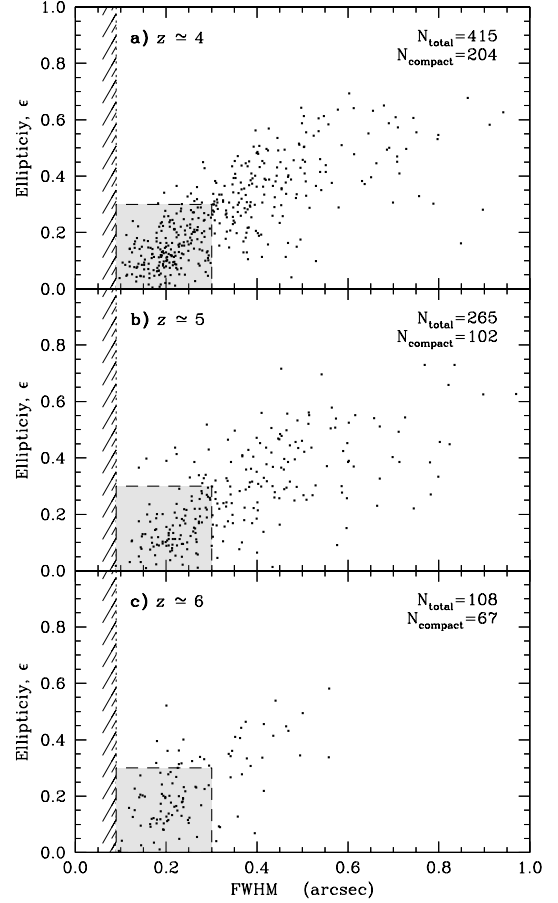


FIG. 2.— Ellipticity, $(1 - b/a)$, versus object FWHM, for all $z \simeq 4$ (a), $z \simeq 5$ (b) and $z \simeq 6$ (c) objects selected in the HUDF. Measurements were performed in i' -band for $z \simeq 4$ and $z \simeq 5$ objects, while we used the z' -band for $z \simeq 6$ objects. The FWHM of a stellar image/PSF is ~ 3 pixels or $0''.09$, indicated by the left-most hatched area in each panel. Objects within the shaded area meet our additional selection criteria on roundness ($\epsilon \leq 0.3$) and compactness ($\text{FWHM} \leq 0''.3$ or 10 pixels).

brightest 54 of these 108 $z \simeq 6$ candidates to $AB = 28.5$ mag. Similarly, deep *HST*/ACS grism spectra of the HUDF i' -band dropouts confirm $\gtrsim 90\%$ of these objects at $AB \lesssim 27.5$ mag to be at $z \simeq 6$ (Malhotra et al. 2005; Hathi et al. 2007). Using the catalog of Yan & Windhorst (2004b), we extracted 108 postage stamps, each 51×51 pixels in size, from the HUDF z' -band image.

Like for the $z \simeq 4$ and $z \simeq 5$ objects, for each $z \simeq 6$ object we measured its z' -band FWHM and ellipticity using *SExtractor*. Figure 2c shows the measured ellipticity versus FWHM for all 108 $z \simeq 6$ candidates. A smaller sample of 67 objects satisfies our constraints on the FWHM and ellipticity. Further visual inspection, to make sure that our sample has only isolated, compact and round objects, leaves 30 objects in our $z \simeq 6$ sample. We therefore imposed a sample size of 30 objects also on the two lower redshift bins after visual inspection.

The results in this paper are therefore based on approximately $(30/415) \sim 7\%$, $(30/265) \sim 11\%$, and $(30/108) \sim 28\%$ of the total $z \simeq 4, 5$ and 6 galaxy populations.

4. RESULTS

4.1. The HUDF Sky Surface-Brightness Level and its rms Variation

For the present work, it is *critical* that we accurately characterize the sky-background, and correctly propagate the true 1σ errors due to the subtraction of this sky-background. In the following, we will pursue two complimentary approaches to determine the sky surface-brightness, and compare the results. Here, we discuss the z' -band measurements in detail.

We first measured the sky-background in each of the 415 $z \simeq 4$ object stamps ('local' sky measurements). The Interactive Data Language (IDL⁵) procedure SKY/MMM.pro⁶ was used to measure the sky-background. This procedure is adapted from the DAOPHOT (Stetson 1987) routine of the same name and works as follows. First, the average and sigma are obtained from the sky pixels. Second, these values are used to eliminate outliers with a low probability. Third, the values are then recomputed and the process is repeated up to 20 iterations. If there is a contamination due to an object, then the contamination is estimated by comparing the mean and median of the remaining sky pixels to get the true sky value. The output of this procedure is the modal sky-level in the image.

Figure 3c shows a histogram of the z' -band modal sky values obtained from all 415 object stamps extracted from the drizzled HUDF images. The 1σ uncertainty in the sky, σ_{sky} , determined from a Gaussian fit to the histogram, is 2.19×10^{-5} electrons sec^{-1} in the z' -band. The sky-background level within the HUDF was obtained from the original flat-fielded ACS images, because the final co-added HUDF data products are sky-subtracted. The header parameters MDRIZSKY and EXPTIME were used to obtain the actually observed sky-value. MDRIZSKY is the sky value in electrons (e^-) computed by the MultiDrizzle code (Koekemoer et al. 2002), while EXPTIME is the total exposure time for the image in seconds, so that the average sky-value in the HUDF has the units of $e^- \text{sec}^{-1}$. Figure 4d shows the histogram of the sky-values obtained from 288 HUDF z' -band flat-fielded exposures. The average value of the sky background, I_{sky} , is $0.02051 e^- \text{sec}^{-1} \text{pix}^{-1}$. That sky-value is measured from the flat-fielded individual ACS images with pixel sizes of $0''.05 \text{ pix}^{-1}$ and hence, in the following calculations, the average sky-value is multiplied by a factor of $(0.030/0.05)^2 = 0.60^2$ to obtain the corresponding average sky-value for the HUDF drizzled pixel size of $0''.030 \text{ pix}^{-1}$. Using these values, we estimate the relative rms random sky-subtraction error as follows:

$$\Sigma_{\text{ss,ran}} = \frac{\sigma_{\text{sky,ran}}}{I_{\text{sky}}} = \frac{2.19 \times 10^{-5}}{2.05 \times 10^{-2} \cdot 0.60^2} = 2.97 \times 10^{-3}$$

The measured average sky background level can then be expressed as the z' -band sky surface brightness as follows:

$$\begin{aligned} \mu_{z'} &= 24.862 - 2.5 \cdot \log \left(\frac{0.0205 \cdot 0.60^2}{0.030^2} \right) \\ &= 22.577 \pm 0.003 \text{ mag arcsec}^{-2} \end{aligned}$$

⁵ IDL Website <http://www.itvis.com/index.asp>

⁶ Part of the IDL Astronomy User's Library, see: <http://idlastro.gsfc.nasa.gov/homepage.html>

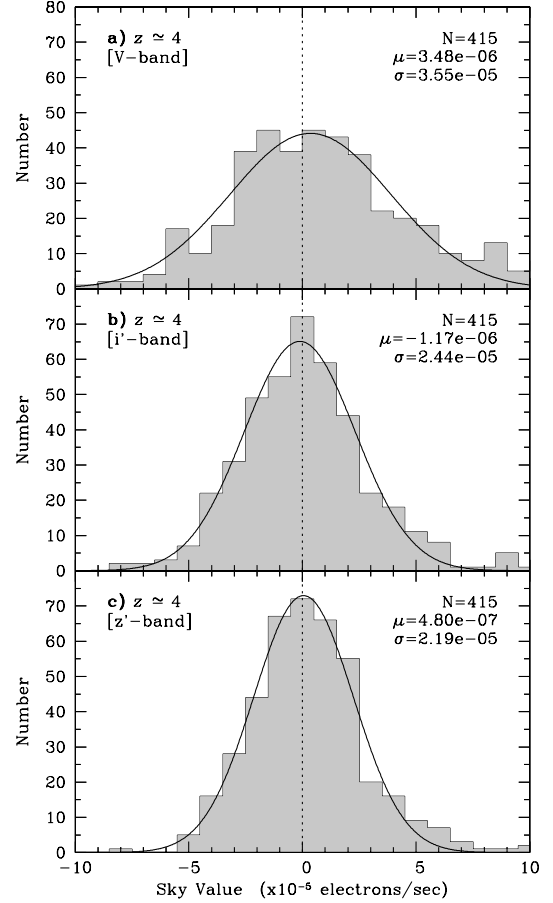


FIG. 3.— Distribution of the modal sky background level used to estimate the 1σ uncertainty in that level, as measured in the 415 $z \simeq 4$ object stamps extracted from the drizzled HUDF images (a) for V-band, (b) for i' -band and (c) for z' -band. The mean (μ) and the sigma (σ) of the best-fit Gaussian to these distributions are also shown in each panel.

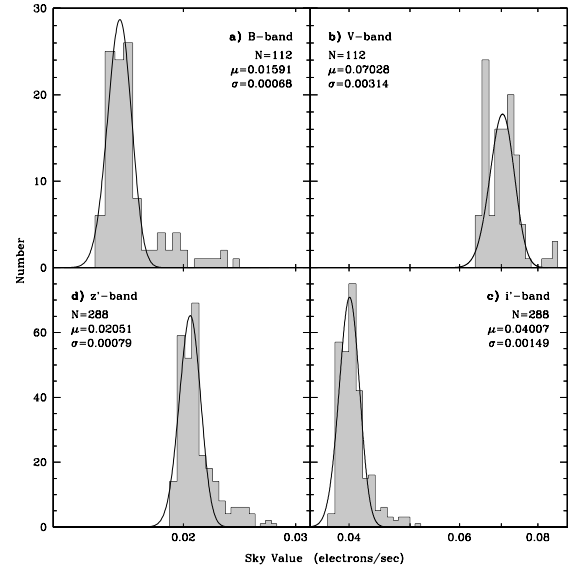


FIG. 4.— The actual sky values measured using header parameters MDRIZSKY and EXPTIME from flat-fielded HUDF exposures. (a) for B-band using 112 exposures. (b) for V-band using 112 exposures. (c) for i' -band using 288 exposures. (d) for z' -band using 288 exposures. The mean (μ) and the sigma (σ) of the best-fit Gaussian to these distributions are shown in each panel.

where 24.862 is the ACS/WFC z' -band AB zero-point, and $0''.030 \text{ pixel}^{-1}$ is the drizzled pixel scale. This is consistent with the values obtained by extrapolating the on-orbit *BVI* sky surface brightness of Windhorst et al. (1994, 1998) to z' , with the sky-background estimates from the ACS Instrument Handbook (Gonzaga et al. 2005), and with the colors obtained by convolving the filter transmission curves with the solar spectrum. Table 1 gives the measured electron detection rate, surface brightness and colors of the sky background with their corresponding errors for the HUDF *BVi'z'* bands as calculated from Figure 3 and Figure 4. The contribution of the zodiacal background dominates the total sky-background, which we find to be only $\sim 10\%$ redder in ($V-i'$) and ($i'-z'$) than the Sun. The z' -band surface brightness corresponding to the 1σ sky-subtraction uncertainty is therefore:

$$\begin{aligned} \mu_{z'} - 2.5 \cdot \log(\Sigma_{\text{ss,ran}}) &= 22.577 - 2.5 \cdot \log(2.97 \times 10^{-3}) \\ &= 28.895 \text{ mag arcsec}^{-2} \end{aligned}$$

Next, we measure the sky-background from 415 ‘blank’ sky stamps (51×51 pixel) distributed throughout the HUDF (‘global’ sky measurements). We measure the sky background using the same IDL algorithm as used above.

Figure 5c shows the histogram of the measured z' -band modal sky values. A Gaussian distribution was fit to this histogram, giving a sky-sigma of $2.00 \times 10^{-5} e^- \text{ sec}^{-1}$. The average value of the sky remains $0.02051 e^- \text{ sec}^{-1}$ (Figure 4d). Using these values, we can estimate a relative rms systematic sky-subtraction error as follows:

$$\Sigma_{\text{ss,sys}} = \frac{\sigma_{\text{sky,sys}}}{I_{\text{sky}}} = \frac{2.00 \times 10^{-5}}{2.05 \times 10^{-2} \cdot 0.60^2} = 2.71 \times 10^{-3}$$

Since the z' -band sky surface brightness remains $22.577 \text{ mag arcsec}^{-2}$, this gives us for the surface brightness corresponding to the 1σ sky subtraction uncertainty:

$$\begin{aligned} \mu_{z'} - 2.5 \cdot \log(\Sigma_{\text{ss,sys}}) &= 22.577 - 2.5 \cdot \log(2.71 \times 10^{-3}) \\ &= 28.995 \text{ mag arcsec}^{-2} \end{aligned}$$

From these two complementary approaches, we can conclude that all surface brightness measurements become unreliable for surface-brightness levels fainter than $28.95 \pm 0.05 \text{ mag arcsec}^{-2}$ in the z' -band. We have also experimented with slightly larger cutouts (75×75 pixels instead of 51×51 pixels) to estimate the sky-subtraction error. We find that with the larger cutouts, the surface brightness corresponding to the 1σ sky-subtraction error is $\sim 0.1-0.2 \text{ mag arcsec}^{-2}$ fainter. For larger cutouts we expect this surface brightness to be $\sim 0.4 \text{ mag}$ fainter but we find about $0.1-0.2 \text{ mag}$ fainter. This might be because of residual systematic errors in the HUDF images. Therefore, we are at the limit of accurately measuring this surface brightness and hence, we will here quote the conservative brighter limit of the surface brightness corresponding to this 1σ sky-subtraction error. Expected contributions to this surface brightness due to uncertainties in the bias level determinations, which correspond to $\sim 0.001 \text{ counts sec}^{-1}$ for typical HUDF exposures (A. M. Koekemoer; private communication), are less than 1%.

Figure 5 clearly shows that the distribution of the modal sky-values is not as symmetric around zero as in Figure 3, and hence, the use of a ‘global’ sky value

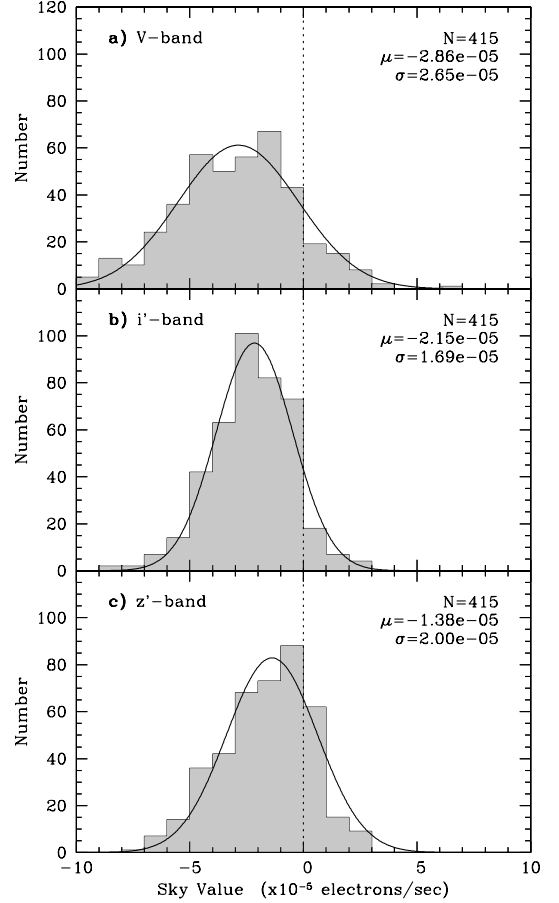


FIG. 5.— Distribution of the modal sky background level used to estimate the 1σ uncertainty in that level, as measured in 415 ‘blank’ 51×51 pixel sky stamps extracted from the drizzled HUDF images (a) for V -band, (b) for i' -band and (c) for z' -band. The mean (μ) and the sigma (σ) of to the best-fit Gaussian to these distributions are shown in each panel.

for the HUDF is not as reliable as ‘local’ sky measurements. Therefore, for the surface brightness profiles and the following discussion, we will adopt the *local* 1σ random sky-subtraction error for all objects in our study.

The average modal sky values and their 1σ errors in the V - and i' -bands were calculated in exactly the same way as for the z' -band, as shown in Figure 3, 4 and 5. The resulting *BVi'z'* sky values and the sky surface-brightness levels are all given in Table 1.

4.2. Composite Images and Surface Brightness Profiles

For each redshift bin ($z \simeq 4, 5, 6$), we generated three ‘stacked’ composite images from subsets of 10 postage stamps that were selected as follows. After placing all 30 image stamps per redshift bin into a $30 \times (51 \times 51)$ pixel IDL array, 10 stamps were randomly drawn without selecting any object more than once. An output image was generated, in which the values at each pixel are the average of the corresponding pixels in the 10 selected input stamps. From the remaining 20 stamps, we again randomly select 10, from which we generated a second composite image, after which the final 10 images were averaged into the third composite image. The three composite images per redshift bin are therefore independent of each other. In none of our realizations did we produce composite images that were essentially unresolved.

TABLE 1
MEASURED SKY VALUES IN $BVi'z'$ (FILTERS) FOR THE HUDF

HUDF Filter	Number of Exposures	Mean Sky Value ^a (e^-/s) and rms error ^b	Sky SB ^c (AB mag arcsec ⁻²)	Sky Color ^c (AB mag)	1 σ Sky-Subtraction error (AB mag arcsec ⁻²)
B	112	0.015909 ± 0.000065	23.664 ± 0.003	$(B - V)_{\text{sky}} = 0.800$	29.85 ± 0.05
V	112	0.070276 ± 0.000297	22.864 ± 0.002	$(V - i')_{\text{sky}} = 0.222$	30.15 ± 0.15
i'	288	0.040075 ± 0.000088	22.642 ± 0.002	$(i' - z')_{\text{sky}} = 0.065$	29.77 ± 0.20
z'	288	0.020511 ± 0.000047	22.577 ± 0.003	$(V - z')_{\text{sky}} = 0.287$	28.95 ± 0.05

^a From Figure 4

^b Error is standard deviation of the mean (σ/\sqrt{N})

^c Sky surface brightness values and colors are consistent with the solar colors in AB mag of $(V-i')=0.19$, $(V-z')=0.21$ and $(i'-z')=0.01$ [except for bluest color ($B-V$)], and is dominated by the zodiacal background.

Even the faintest $z \simeq 4-6$ galaxies are clearly resolved. The $z \simeq 4, 5, 6$ objects used to generate the composite images have an apparent magnitude range of approximately 27.5 ± 1.0 AB mag. Because the magnitude range is relatively small and the S/N per pixel is low even in their central pixel, we have given all objects equal weight. To test whether this range in magnitude will affect our stacks and hence, our profiles, we created 3 stacks depending on the apparent magnitude, i.e. one stack of the 10 brightest objects in the sample, a second stack of the 10 next brightest objects in the sample and a third stack of the 10 faintest objects in the sample. This is summarized in Figure 6d. We found that the profiles were very similar except that the profiles of the fainter stacks fall-off more quickly at larger radius compared to the profile of the brightest stack, but the inner profile and the deviation in the profiles are clearly visible in all 3 stacks. Therefore, we conclude that for our range in apparent magnitudes, our stacks/profiles are not affected. Perhaps most surprisingly, Figure 6d shows that r_e value of all 3 flux ranges ($\sim 26.0-27.0$, $\sim 27.0-28.0$ & $\sim 28.0-29.0$ mag) are all about the same over $\sim 3-4$ mag in flux, so the primary parameter that distinguishes the brighter from the fainter $z \simeq 6$ dropouts is their central surface brightness (which thus also varies by $\sim 3-4$ mag).

We used the IRAF⁷ procedure ELLIPSE to fit surface brightness profiles shown in Figure 6 to each of the three independent composite images per redshift bin. We also computed a mean surface-brightness profile from the three composite surface brightness profiles generated from the three independent composite images for each redshift bin. Figure 7 shows composite images for $z \simeq 4, 5, 6$ objects. Here each composite image is a stack of 30 objects. Figure 8 shows the average surface brightness profiles for each of the redshift intervals $z \simeq 4, 5, 6$. The thin solid curves in Figure 6 and the dot-dash curves in Figure 8 represent the observed ACS V , i' and z' -band Point Spread Functions (PSFs), while the horizontal dashed lines indicate the surface brightness level corresponding to the 1σ sky-subtraction error in each of the HUDF images as discussed in § 4.1. It is important to note that we scaled the ACS PSFs to match the surface brightness of the central data point in our mean surface-brightness profile, to determine how extended the mean surface-brightness profile is with respect to the PSFs.

⁷ IRAF (<http://iraf.net>) is distributed by the National Optical Astronomy Observatories, which are operated by the Association of Universities for Research in Astronomy, Inc., under cooperative agreement with the National Science Foundation.

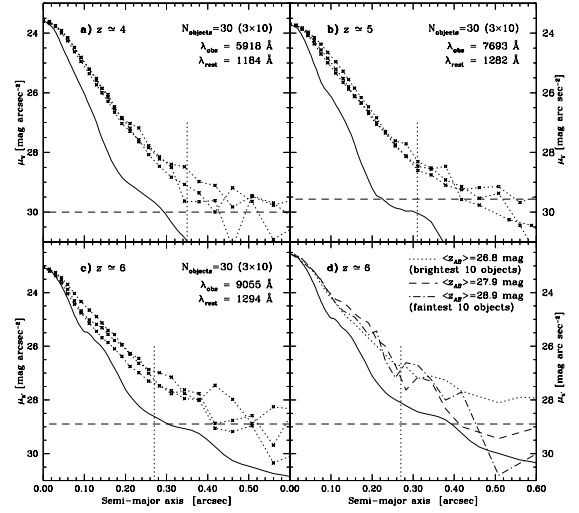


FIG. 6.— Composite surface brightness profiles for three independent sets of 10 objects at (a) $z \simeq 4$, (b) $z \simeq 5$ and (c) $z \simeq 6$, respectively. The thin solid curve represents the ACS V , i' and z' -band PSFs, respectively, while the horizontal dashed line indicates the surface brightness level corresponding to the 1σ sky-subtraction error in the HUDF images. The vertical dotted line marks the radius at which the profile starts to deviate significantly from the extrapolation of the inner $r^{1/n}$ profile observed at smaller radii. Note that at $z \simeq 6$, this deviation is still well above the red z' -band PSF halo at $r \gtrsim 0''.30$. The panel (d) shows 3 $z \simeq 6$ composite profiles (each with a set of 10 objects) divided by apparent magnitudes. The brightest composite profile (dotted) has an average z' -band magnitude of ~ 26.8 mag. The next brightest composite profile (short dash) has an average z' -band magnitude of ~ 27.9 mag, and the faintest composite profile (dot-dash) has an average z' -band magnitude of ~ 28.9 mag.

In Figure 8, we fitted all possible combinations of the Sérsic profiles (convolved with the ACS PSF) to the observed profiles and using χ^2 minimization, found the best fits for galaxies at $z \simeq 4, 5, 6$. The best fit Sérsic index (n) for all three profiles ($z \simeq 4, 5, 6$) is $n < 2$, meaning these galaxies follow mostly exponential disk-type profiles in their central regions. We find that the observed profiles start to deviate from the best-fit profiles at $r \gtrsim 0''.27$, somewhat depending on the redshift. From Figure 8, we also see that in each of V ($z \simeq 4$), i' ($z \simeq 5$) and z' ($z \simeq 6$), the PSF declines more rapidly with radius than the composite radial surface brightness profile for $r \gtrsim 0''.27$. It is therefore unlikely that the observed ‘breaks’ result from the halos and structure of the ACS PSFs. Specifically, at $z \simeq 6$ the most significant deviations in the light-profiles are seen at levels 1.5–2.0 mag above the 1σ sky-subtraction error, and well above the

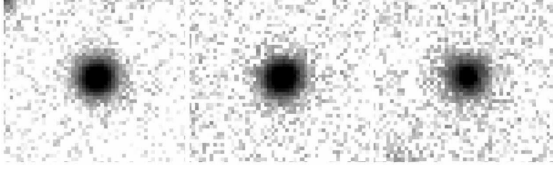


FIG. 7.— Composite images for **Left** $z \simeq 4$, **Center** $z \simeq 5$ and **Right** $z \simeq 6$ objects. Here each composite image is a stack of 30 objects. Each stamp is $1''/53$ on a side.

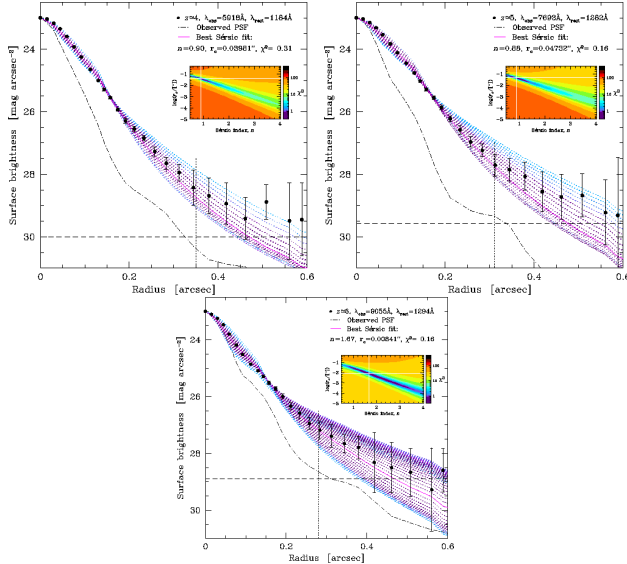


FIG. 8.— Mean surface brightness profiles with a best fit Sérsic profiles for 30 composite images at (a) $z \simeq 4$, (b) $z \simeq 5$ and (c) $z \simeq 6$, respectively. The thin dot-dash curve represents the ACS V, i' and z' -band PSFs, respectively, while the horizontal dashed line indicates the surface brightness level corresponding to the 1σ sky-subtraction error in the HUDF images. The vertical dotted line marks the radius at which the profile starts to deviate significantly from the extrapolation of the inner $r^{1/n}$ profile observed at smaller radii. The n and r_c are the best fit Sérsic parameters.

PSF wings. Each of the mean surface brightness profiles display a well-defined break, the radius of which appears to change somewhat with redshift. The vertical dotted lines (in Figure 6 and Figure 8) mark the radius at which the mean surface brightness profiles start to deviate significantly from the extrapolation of the $r^{1/n}$ profile observed at smaller radii.

4.3. Test of the Stacking Technique on Nearby Galaxies

To test the general validity of the stacking technique itself on a local galaxy sample, we used surface photometry from the Nearby Field Galaxy Survey (NFGS; Jansen et al. 2000a,b). The NFGS sample contains 196 nearby galaxies, that were objectively selected from the CfA redshift catalog (CfA I; Davis & Peebles 1983; Huchra et al. 1983) to span the full range in absolute B magnitude present in the CfA I ($-14.7 \lesssim M_B \lesssim -22.7$ mag). The absolute magnitude distribution in the NFGS sample approximates the local galaxy luminosity function (e.g., Marzke et al. 1994), while the distribution over Hubble type follows the changing mix of morphological types as a function of luminosity in the local galaxy population. The NFGS sample (as detailed in Jansen et al. 2000a) minimizes biases, and yields a sample that, with very few caveats, is representative of the local galaxy

population. As part of the NFGS, UBR surface photometry, both integrated (global) and nuclear spectrophotometry, as well as internal kinematics were obtained (see Jansen & Kannappan 2001). Here, we will concentrate on the U -band surface photometry, since it is closest in wavelength to the rest-frame wavelengths observed at $z \simeq 4-6$. Although, ideally, we would want a filter further into the UV, Taylor et al. (2007) and Windhorst et al. (2002) show that for the majority of late-type nearby galaxies, the apparent structure of galaxies does not change dramatically once one observes shortward of the Balmer break. Early-type galaxies, however, are a clear exception to this, but these are not believed to dominate the galaxy population at $z \simeq 4-6$, as discussed before.

Figure 9 shows stacked profiles for relatively luminous early-, spiral-, and late-type galaxies drawn from the NFGS. Vertical dotted lines indicate the half-light radii and their intersection with the profiles, the surface brightness at that radius. Dashed lines indicate exponential fits to the outer portion of each profile. Figure 9 also shows that co-adding profiles for disparate morphological types and for mid-type spiral galaxies with a range in bulge-to-disk ratios can produce breaks in the composite profile. No such breaks are seen when the profiles of either early-type galaxies (E, S0) or late-type galaxies (Sd-Irr) are co-added. This figure shows that, *if* galaxies at $z \simeq 4-6$ had similar morphological types as local galaxies, then it would be possible to produce a break in the profiles (as shown in Figure 6 and Figure 8), merely by mixing different types of galaxies. We do not believe that the galaxy populations at $z \simeq 4-6$ morphologically resemble those at low redshift. Hence, for primarily late-type galaxies, which dominate the faint blue galaxy population at $AB \geq 24$ mag (Driver et al. 1998), and which likely dominate the fainter end of the luminosity function at $z \simeq 4-6$ that we sample here (Yan & Windhorst 2004a,b), the image stacking is likely a valid exercise.

The primary goal of this section was to show that the profile stacking technique is valid and can be used to get meaningful surface brightness profiles. We are not comparing our nearby sample with galaxies at $z \simeq 4-6$. These nearby galaxies are unlikely to be local analogues of high redshift galaxies. If we apply surface brightness dimming to UV light-profiles of these nearby galaxies, they would be mostly invisible to *HST*, and in some cases visible to *JWST* in long integration (see e.g. Windhorst et al. 2006). This is another way of saying that the $z \simeq 4-6$ objects are truly different from $z \simeq 0$ objects.

5. DISCUSSIONS

Figure 8 shows that the mean surface brightness profiles deviate significantly from an inner $r^{1/n}$ profile at radii $r \gtrsim 0''.27-0''.35$, depending somewhat on the redshift bin. These deviations appear real, with the break/point of departure located $\gtrsim 1.5-2$ mag above the 1σ sky-subtraction error and above the PSF-wings. In the following, we discuss several possible explanations for the observed shapes of our composite surface brightness profiles.

5.1. Galaxies with Different Morphologies

Our test on nearby galaxies (Figure 9) shows that, if we stack many galaxies with different morphologies (early-type, late-type or spiral galaxies), it is possible to get a

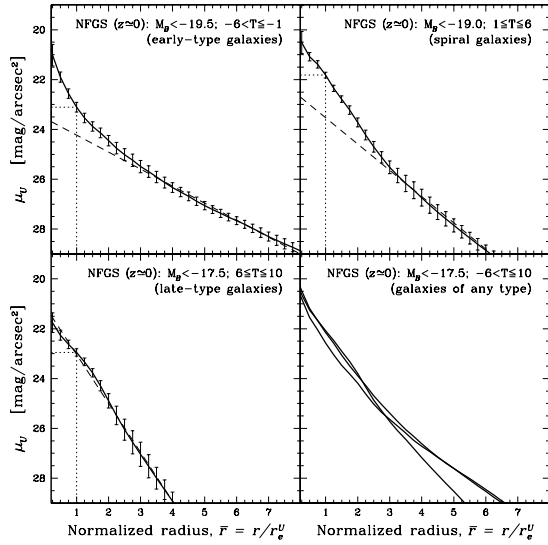


FIG. 9.— Stacked radial surface brightness profiles for relatively luminous early-, spiral- and late-type nearby galaxies drawn from the Nearby Field Galaxy Survey (Jansen et al. 2000a,b). The vertical dotted line indicates the half-light radius, while the dashed line represents an exponential fit to the outer portions of each composite profile. Co-adding profiles for disparate morphological types and for spiral galaxies with a range in bulge-to-disk ratios can produce breaks in the composite profile. No significant breaks are seen in the *outer* light profiles, when the profiles of either early-type galaxies (E, S0) or late-type galaxies (Sd-Irr) are co-added.

slope-change (‘break’) in the average surface brightness profile. Ravindranath et al. (2006) find that 40% of the brighter LBGs at $2.5 < z < 5$ have light profiles close to exponential, as seen for disk galaxies, and only $\sim 30\%$ have high n , as seen in nearby spheroids. They also find a significant fraction ($\sim 30\%$) of galaxies with light profiles *shallower* than exponential, which appear to have multiple cores or disturbed morphologies, suggestive of close pairs or on-going galaxy mergers. Therefore, if galaxies at $z \simeq 4-6$ have a variety of morphological types, then the shape of the average surface brightness profile that we see may be due to the stacking of different types of galaxies. Therefore, we find that the exponential and the flatter profiles found by Ravindranath et al. (2006) for galaxies at $2.5 < z < 5$ also apply to higher redshifts ($z \geq 5$).

Also, we believe that it is more likely that the high redshift, faint galaxy population consists primarily of small galaxies with late-type morphologies and with sub- L^* luminosities, as seen at $z \simeq 2-3$ (Driver et al. 1995, 1998). So if the $z \simeq 4-6$ population consists of such a late-type galaxy population, then the slope-change in the light profiles is likely not the result of co-adding images of objects with disparate morphological types.

5.2. Central Star Formation/Starburst

HST optical images of galaxies at $z \simeq 4-6$ sample their rest-frame UV ($\sim 1200 \text{ \AA}$), where the contribution from the actively star-forming regions (very young, massive stars) dominates the UV-light. Hathi et al. (2007) have shown that galaxies at $z \simeq 5-6$ are high redshift starbursts and these galaxies have similar starburst intensity limit as local starbursting galaxies. Therefore, it is possible that galaxies at $z \simeq 4-6$ have centrally concentrated star formation or starburst. This possibil-

ity is based on three key assumptions: (1) most of the galaxies at $z \simeq 4, 5, 6$ are intrinsically later-type galaxies (Driver et al. 1998; Steidel et al. 1999); (2) the Spectral Energy Distribution (SED) of these galaxies at $z \simeq 4, 5, 6$ are dominated by early A- to late O-type stars, respectively; and (3) there are no old stars with ages at $z \simeq 4-6$ greater than 2-1 Gyr in WMAP cosmology, respectively.

Hunter & Elmegreen (2006) studied azimuthally averaged surface photometry profiles for large sample of nearby irregular galaxies. They find some galaxies have double exponentials that are steeper (and bluer) in the inner parts compared to outer parts of the galaxy. Hunter & Elmegreen (2006) discuss that this type of behavior is expected in galaxies where the centrally concentrated star formation or starburst steepens the surface brightness profiles in the center. If that is the case, then one might expect a better correlation between the break in the surface brightness profiles and changes in color profiles. Unfortunately, for our sample of galaxies at $z \simeq 4-6$, we don’t have high-resolution restframe *UBV* color information. The objects are generally too faint for *Spitzer Space Telescope*, and hence we cannot confirm or reject this possibility for the shape of our composite surface brightness profiles.

5.3. Limits to Dynamical Ages for $z \simeq 4, 5, 6$ Objects

The average compact $z \simeq 4-6$ galaxy is clearly extended with respect to the ACS PSFs (Figure 8), and is best fit by an exponential profile ($n < 2$) out to a radius of about $r \simeq 0''.35, 0''.31$, and $0''.27$ at $z \simeq 4, 5$ and 6, respectively. The apparent progression with redshift is noteworthy. The radius at which the profile starts to deviate from $r^{1/n}$ (in this case at radius $r \gtrsim 0''.35-0''.27$) may be an important constraint to the dynamical time scale of the system, as discussed in § 1. If this argument is valid, then we can estimate limits to the dynamical ages of $z \simeq 4, 5, 6$ galaxies as follows.

In WMAP cosmology, a radius of $r \gtrsim 0''.35$ at $z \simeq 4$ corresponds to $r \gtrsim 2.5$ kpc. The dynamical time scale (e.g., Binney & Tremaine 1987), τ_{dyn} , goes as $\tau_{dyn} = Cr^{3/2}/\sqrt{GM}$, where the constant $C = \pi/2$. For a typical dwarf galaxy mass range of $\sim 10^9-10^8 M_\odot$ inside $r=2.5$ kpc, we infer that the limits to the dynamical age would be $\tau_{dyn} \simeq 90-290$ Myr, which is the lifespan expected for a late-type B-star. This means that the last major merger that affected this surface brightness profile and that triggered its associated starburst may have occurred ~ 0.20 Gyr before $z \simeq 4$, —assuming that the star-formation wasn’t spontaneous, but associated with some accretion or a merging event.

Table 2 shows the break-radius and inferred limits to dynamical ages for the $z \simeq 4-6$ objects. At $z \simeq 5$, we find that the limits to dynamical age at the break radius would be $\tau_{dyn} \simeq 70-210$ Myr, which is the lifespan expected for a mid B-star, while at $z \simeq 6$, $\tau_{dyn} \simeq 50-150$ Myr, which is the lifespan expected for a late O-early B-star. This means that the last major merger that affected these surface brightness profiles at $z \simeq 5$ and 6 and that triggered its associated starburst may have occurred ~ 0.14 and ~ 0.10 Gyr before $z \simeq 5$ and 6, respectively.

The dynamical time is a lower limit to the actual time available, since it assumes matter starts from rest. Any angular momentum at start will increase the available

TABLE 2
DYNAMICAL AGES FOR $z \simeq 4-6$ OBJECTS IN THE HUDF

Redshift z	“Break” Radius ^a (arcsec)	“Break” Radius ^b (kpc)	Dynamical Age ^c (τ_{dyn})
4	0.35	2.5	0.09–0.29 Gyr
5	0.31	2.0	0.07–0.21 Gyr
6	0.27	1.6	0.05–0.15 Gyr

^a From composite surface brightness profiles (Figure 6 and Figure 8).

^b Radius in kpc corresponding to radius in arcsec at given redshift.

^c If “break radius” interpreted as indicator of dynamical age.

time. The best-fit SED age from the GOODS *HST* and *Spitzer* photometry on some of the brighter of these objects — using Bruzual & Charlot (2003) templates — is in the range of about $\sim 150-650$ Myr (Yan et al. 2005; Eyles et al. 2005, 2007), the lower end of which is consistent with our limits to their dynamical age estimates, while the somewhat larger SED ages could also be affected by the onset of the AGB in the stellar population increasing the observed *Spitzer* fluxes and hence possibly overestimating ages (Maraston 2005). Our age estimates for $z \simeq 4-6$ are consistent with the trend of SED ages suggested for $z \simeq 7$ (Labbé et al. 2006). It is noteworthy that, given the uncertainties, the two independent age estimates are consistent. If our limits to dynamical age estimates for the image *stacks* are thus valid, they are consistent with the SED ages, and point to a consistent young age for these objects.

Furthermore, the presence of young, massive late O–early B-stars at $z \simeq 6$ has implications for the reionization of the universe. From observations of the appearance of complete Gunn-Peterson troughs in the spectra of $z \gtrsim 5.8$ quasars (Fan et al. 2006), we know that the epoch of reionization had ended by $z \simeq 6$. From the steep ($\alpha = -1.8$) faint-end slope of the luminosity function of $z \simeq 6$ galaxies, Yan & Windhorst (2004a,b) concluded that dwarf galaxies, and not quasars, likely finished reionization by $z \simeq 6$. Should the present interpretation of their light profiles be correct, then it would appear to add support to this picture, in the sense that such objects are dominated by B-stars and did not start their most recent major starburst long before $z \simeq 6$.

6. SUMMARY

We used the stacked HUDF images to analyze the average surface brightness profiles of $z \simeq 4-6$ galaxies. Our analysis shows that even the faintest galaxies at $z \simeq 4-6$ are resolved. This may have implications on the stellar density and its relation to the stellar density in present-day galaxies. We also find that the average surface brightness profiles display breaks at a radius that progresses toward lower redshift from $r \simeq 0''.27$ (1.6 kpc) at $z \simeq 6$ to $r \simeq 0''.35$ (2.5 kpc) at $z \simeq 4$.

The shape of the radial surface brightness profile that we observe could result from a mixture of different morphological types of galaxies, if they exist at $z \simeq 4-6$, because we can produce similar breaks in the surface brightness profiles when we mix different types of nearby galaxies. Alternatively, if these galaxies are dominated by a central starburst then they could show such double exponential-type profiles, as discussed by Hunter & Elmegreen (2006). In a third scenario, if the galaxies at $z \simeq 4-6$ are truly young and mostly late-type, the outer profiles seen in our mean radial surface brightness profiles at $z \simeq 4-6$ bear the imprint of the hierarchical build-up process, and are still dominated by infalling material, which is *not* detectable in the individual HUDF images of these faint objects. We have estimated limits to dynamical ages from the break radius at $z \simeq 4, 5, 6$, very roughly as $\sim 0.20, 0.14$ and 0.10 Gyr, respectively, and those ages are similar to the SED ages inferred at $z \simeq 4-6$ (Yan et al. 2005; Eyles et al. 2005, 2007), and consistent with SED ages suggested for $z \simeq 7$ (Labbé et al. 2006). Hence, at $z \simeq 4, 5, 6$, the last major merger that affected the surface brightness profiles that we observe, and that triggered the observed star-burst, may have occurred respectively $\sim 0.20, 0.14$ and 0.10 Gyr earlier, or very approximately at $z \simeq 4.5, 5.5, 6.5$. This would be consistent with the hierarchical assembly of galaxies and with the end of reionization, since it would imply that from $z \simeq 4$ to $z \simeq 6$, the SEDs become progressively more dominated by late-B–late-O stars. This implies that the sub- L^* (i.e. dwarf) galaxies may have produced sufficient numbers of energetic UV photons to complete the reionization process by $z \simeq 6$, as Yan & Windhorst (2004a,b) suggested. It will be imperative to study with future instruments like *HST*/WFC3 and *JWST* (Windhorst et al. 2006, 2007) whether the dominant stellar population indeed changes from late-O–early-B at $z \simeq 6$ (i.e. capable of reionizing) to mid- to late-B at $z \simeq 4-5$ (i.e. capable of maintaining reionization), and to what extent the intrinsic sizes of these faint objects will ultimately limit deep *JWST* surveys.

This work was partially supported by HST grants AR 10298 and GO 9780 from the Space Telescope Science Institute, which is operated by AURA under NASA contract NAS 5-26555. The authors thank Deidre Hunter, Alan Dressler, Henry Ferguson, Anton Koekemoer, Robert Morgan for their helpful discussions. RAW acknowledges support from NASA JWST Interdisciplinary Scientist grant NAG5-12460 from GSFC, that supported an investigation of the implications of this work for JWST. We specially thank our referee, Dr. Patrick McCarthy, for his helpful comments that have improved this paper.

Facilities: HST(ACS)

REFERENCES

- Beckwith, S., Stiavelli, M., Koekemoer, A. M., et al. 2006, *AJ*, 132, 1729
 Bertin, E., & Arnouts, S. 1996, *A&AS*, 117, 393
 Binney, J. J., & Tremaine, S. 1987, *Galactic Dynamics* (Princeton: Princeton Univ. Press)
 Bolzonella, M., Miralles, J. M., & Pelló, R. 2000, *A&A*, 363, 476
 Bouwens, R., Illingworth, G. D., Thompson, R. I., et al. 2004, *ApJ*, 606, L25
 Bouwens, R. J., Illingworth, G. D., Blakeslee, J. P., & Franx, M. 2006, *ApJ*, 653, 53
 Bouwens, R. J., Illingworth, G. D., Franx, M., & Ford, H. 2007, *ApJ*, in press (astro-ph/0707.2080)
 Brandt, W. N., Hornschemeier, A. E., Schneider, D. P., Alexander, D. M., Bauer, F. E., Garmire, G. P., & Vignali, C. 2001, *ApJ*, 558, L5
 Bruzual, G., & Charlot, S. 2003, *MNRAS*, 344, 1000
 Bunker, A. J., & Stanway, E. R. 2004, (astro-ph/0407562)

- Cowie, L. L., Songaila, A., Hu, E. M., & Cohen, J. G. 1996, *AJ*, 112, 839
- Davis, M., & Peebles, P. J. M. 1983, *ApJ*, 267, 465
- Dow-Hygelund, C., Holden, B., Bouwens, R., et al. 2007, *ApJ*, 660, 47
- Driver, S. P., Windhorst, R. A., & Griffiths, R. E. 1995, *ApJ*, 453, 48
- Driver, S. P., Fernandez-Soto, A., Couch, W. J., Odewahn, S. C., Windhorst, R. A., Phillips, S., Lanzetta, K., & Yahil, A. 1998, *ApJ*, 496, L93
- Eyles, L. P., Bunker, A. J., Stanway, E. R., Lacy, M., Ellis R. S., & Doherty, M. 2005, *MNRAS*, 364, 443
- Eyles, L. P., Bunker, A. J., Ellis R. S., Lacy, M., Stanway, E. R., Stark, D., & Chiu, K. 2007, *MNRAS*, 374, 910
- Fan, X., Strauss, M. A., Becker, R. H., et al. 2006, *AJ*, 132, 117
- Georgakakis, A., Hopkins, A. M., Sullivan, M., Afonso, J., Georgantopoulos, I., Mobasher, B., & Cram, L. E. 2003, *MNRAS*, 345, 939
- Giavalisco, M., Dickinson, M., Ferguson, H. C., et al. 2004, *ApJ*, 600, L103
- Gonzaga, S., et al. 2005, “ACS Instrument Handbook”, Version 6.0, (Baltimore:STScI)
- Guzman, R., Gallego, J., Koo, D. C., Phillips, A. C., Lowenthal, J. D., Faber, S. M., Illingworth, G. D., & Vogt, N. P. 1997 *ApJ*, 489, 559
- Hathi, N. P., Malhotra, S., & Rhoads, J. E. 2007, *ApJ*, submitted (astro-ph/0709.0520)
- Heavens, A., Panter, B., Jimenez, R., & Dunlop, J. 2004, *Nature*, 428, 625
- Hu, E. M., Cowie, L. L., McMahon, R. G., Capak, P., Iwamuro, F., Kneib, J.-P., Maihara, T., & Motohara, K. 2002, *ApJ*, 568, L75
- Huchra, J. P., Davis, M., Latham, D., & Tonry, J. 1983, *ApJS*, 52, 89
- Hunter, D. A., & Elmegreen, B. G. 2006, *ApJS*, 162, 49
- Jansen, R. A., Franx, M., Fabricant, D., & Caldwell, N. 2000a, *ApJS*, 126, 271
- Jansen, R. A., Fabricant, D., Franx, M., & Caldwell, N. 2000b, *ApJS*, 126, 331
- Jansen, R. A. & Kannappan, S. J. 2001, *Ap&SS*, 276, 1151
- Kodaira, K., Taniguchi, Y., Kashikawa, N., et al. 2003, *PASJ*, 55, L17
- Kodama, T., Yamada, T., Akiyama, M., et al. 2004, *MNRAS*, 350, 1005
- Koekemoer, A. M., Fruchter, A. S., Hook, R. N., & Hack, W. 2002, *The 2002 HST Calibration Workshop*, ed. S. Arribas, A. Koekemoer, and B. Whitmore (Baltimore:STScI), 337
- Kormendy, J. 1977, *ApJ*, 218, 333
- Kurk, J. D., Cimatti, A., di Serego A. S., Vernet, J., Daddi, E., Ferrara, A., & Ciardi, B. 2004, *A&A*, 422, L13
- Labbé, I., Bouwens, R., Illingworth, G. D., & Franx, M. 2006, *ApJ*, 649, L67
- Lynden-Bell, D. 1967, *MNRAS*, 136, 101
- Maraston, C. 2005, *MNRAS*, 362, 799
- Malhotra, S., Rhoads, J. E., Pirzkal, N., et al. 2005, *ApJ*, 626, 666
- Marzke, R. O., Huchra, J. P. & Geller, M. J. 1994, *ApJ*, 428, 43
- McCarthy, P. J. 2004, *BAAS*, 36, 1555
- Nandra, K., Mushotzky, R. F., Arnaud, K., Steidel, C. C., Adelberger, K. L., Gardner, J. P., Teplitz, H. I., & Windhorst, R. A. 2002, *ApJ*, 576, 625
- Oke, J. B., & Gunn, J. E. 1983, *ApJ*, 266, 713
- Panther, B., Jimenez, R., Heavens, A. F., & Charlot, S. 2007, *MNRAS*, 378, 1550
- Pascarelle, S. M., Windhorst, R. A., Keel, W. C., & Odewahn, S. C. 1996, *Nature*, 383, 45
- Ravindranath, S., Giavalisco, M., Ferguson, H. C., et al. 2006, *ApJ*, 652, 963
- Rhoads, J. E., Xu, C., Dawson, S., et al. 2004, *ApJ*, 611, 59
- Spergel, D. N., Bean, R., Doré, O., et al. 2007, *ApJS*, 170, 377
- Steidel, C. C., Adelberger, K. L., Giavalisco, M., Dickinson, M., & Pettini, M. 1999, *ApJ*, 519, 1
- Stern, D., Yost, S. A., Eckart, M. E., Harrison, F. A., Helfand, D. J., Djorgovski, S. G., Malhotra, S., & Rhoads, J. E. 2005, *ApJ*, 619, 12
- Stetson, P. B. 1987, *PASP*, 99, 191
- Taniguchi, Y., Ajiki, M., Nagao, T., et al. 2005, *PASJ*, 57, 165
- Taylor, V. A., Conselice, C. J., Windhorst, R. A., & Jansen, R. A. 2007, *ApJ*, 659, 162
- van Albada, T. S. 1982, *MNRAS*, 201, 939
- van Dokkum, P. G., Förster, S., Natascha, M., et al. 2003, *ApJ*, 587, L83
- van Dokkum, P. G., Franx, M., Förster, S., et al. 2004, *ApJ*, 611, 703
- Vanzella, E., Cristiani, S., Dickinson, M., et al. 2006, *A&A*, 454, 423
- White, R. L., Helfand, D. J., Becker, R. H., Glikman, E., & de Vries, W. 2007, *ApJ*, 654, 99
- Williams, R. E., Blacker, B., Dickinson, M., et al. 1996, *AJ*, 112, 1335
- Windhorst, R. A., Gordon, J. M., Pascarelle, S. M., Schmidtke, P. C., Keel, W. C., Burkey, J. M., & Dunlop, J. S. 1994, *ApJ*, 435, 577
- Windhorst, R. A., Keel, W. C., & Pascarelle, S. M. 1998, *ApJ*, 494, 27
- Windhorst, R. A., Taylor, V. A., Jansen, R. A., et al. 2002, *ApJS*, 143, 113
- Windhorst, R. A., Cohen, S. H., Jansen, R. A., Conselice, C., & Yan, H. 2006, *NewAR*, 50, 113
- Windhorst, R. A., Hathi, N. P., Cohen, S. H., & Jansen, R. A. 2007, *Advances in Space Research*, in press (astro-ph/0703171)
- Yan, H. & Windhorst, R. 2004a, *ApJ*, 600, L1
- Yan, H. & Windhorst, R. 2004b, *ApJ*, 612, L93
- Yan, H., Dickinson, M., Stern, D., et al. 2005, *ApJ*, 634, 109
- York, D. G., et al. 2000, 120, 1579
- Zibetti, S., White, S. D. M., & Brinkmann, J. 2004, *MNRAS*, 347, 556